Acta Pharmaceutica Sinica B 2025;15(2):681−691

Chinese Pharmaceutical Association
Institute of Materia Medica, Chinese Academy of Medical Sciences

Acta Pharmaceutica Sinica B

www.elsevier.com/locate/apsb
www.sciencedirect.com

ORIGINAL ARTICLE

L-[5-^{11}C]Glutamine PET imaging noninvasively tracks dynamic responses of glutaminolysis in non-alcoholic steatohepatitis

Yiding Zhang[a,†], Lin Xie[a,*,†], Masayuki Fujinaga[a,†], Yusuke Kurihara[a,b], Masanao Ogawa[a,b], Katsushi Kumata[a], Wakana Mori[a], Tomomi Kokufuta[a], Nobuki Nengaki[a], Hidekatsu Wakizaka[a], Rui Luo[a,c], Feng Wang[c], Kuan Hu[d], Ming-Rong Zhang[a,*]

[a]*Department of Advanced Nuclear Medicine Sciences, Institute for Quantum Medical Science, National Institutes for Quantum Science and Technology, Chiba 263-8555, Japan*
[b]*SHI Accelerator Service, Ltd, Tokyo 141-0031, Japan*
[c]*Department of Nuclear Medicine, Nanjing First Hospital, Nanjing Medical University, Nanjing 210006, China*
[d]*State Key Laboratory of Bioactive Substance and Function of Natural Medicines, Institute of Materia Medica, Chinese Academy of Medical Sciences & Peking Union Medical College, Beijing 100050, China*

Received 15 March 2024; received in revised form 7 June 2024; accepted 26 July 2024

KEY WORDS

L-[5-^{11}C]Glutamine;
Positron emission tomography;
Non-alcoholic steatohepatitis;
Glutaminolysis;
Glutaminase 1;
Metabolic intervention;
BPTES therapy

Abstract Inhibiting glutamine metabolism has been proposed as a potential treatment strategy for improving non-alcoholic steatohepatitis (NASH). However, effective methods for assessing dynamic metabolic responses during interventions targeting glutaminolysis have not yet emerged. Here, we developed a positron emission tomography (PET) imaging platform using L-[5-^{11}C]glutamine ([^{11}C]Gln) and evaluated its efficacy in NASH mice undergoing metabolic therapy with bis-2-(5-phenylacetamido-1,3,4-thiadiazol-2-yl)ethyl sulfide (BPTES), a glutaminase 1 (GLS1) inhibitor that intervenes in the first and rate-limiting step of glutaminolysis. PET imaging with [^{11}C]Gln effectively delineated the pharmacokinetics of L-glutamine, capturing its temporal-spatial pattern of action within the body. Furthermore, [^{11}C]Gln PET imaging revealed a significant increase in hepatic uptake in methionine and choline deficient (MCD)-fed NASH mice, whereas systemic therapeutic interventions with BPTES reduced the hepatic avidity of [^{11}C]Gln in MCD-fed mice. This reduction in [^{11}C]Gln uptake correlated with a decrease in

*Corresponding authors.
E-mail addresses: xie.lin@qst.go.jp (Lin Xie), zhang.ming-rong@qst.go.jp (Ming-Rong Zhang).
[†]These authors made equal contribution to this work.
Peer review under the responsibility of Chinese Pharmaceutical Association and Institute of Materia Medica, Chinese Academy of Medical Sciences.

https://doi.org/10.1016/j.apsb.2024.07.023

GLS1 burden and improvements in liver damage, indicating the efficacy of BPTES in mitigating NASH-related metabolic abnormalities. These results suggest that [^{11}C]Gln PET imaging can serve as a noninvasive diagnostic platform for whole-body, real-time tracking of responses of glutaminolysis to GLS1 manipulation in NASH, and it may be a valuable tool for the clinical management of patients with NASH undergoing glutaminolysis-based metabolic therapy.

1. Introduction

L-Glutamine, a nonessential/conditionally essential amino acid, plays crucial roles in various metabolic pathways, including energy production, amino acid synthesis, and the regulation of oxidative stress[1,2]. Dysfunctional glutamine metabolism is recognized as a hallmark of non-alcoholic steatohepatitis (NASH), a significant global health concern and a risk factor for cirrhosis, liver cancer, and cardiovascular diseases, with no currently approved therapies. This suggests that interventions targeting glutaminolysis could hold promise as anti-NASH therapies[3,4]. Furthermore, recent observations have highlighted the protective effects of glutaminolysis-based metabolic therapy in liver disease[4,5], cardiovascular disease[6,7], and cancer[8–10]. Glutaminase (GLS), a rate-limiting enzyme responsible for converting L-glutamine to glutamate and ammonia, exhibits two distinct isoforms in mammalian tissues, namely GLS1 and GLS2, originating from separate but structurally related genes. In healthy individuals, GLS1 is prevalent across various extra-hepatic tissues, while GLS2 is notably abundant in the normal adult liver[11]. Notably, a metabolic switch from GLS2 to GLS1 occurs in live fibrosis[5], cirrhosis and liver cancer[12–14], as evidenced by studies involving hepatic biopsies from NASH patients and murine NASH models[4]. Furthermore, inhibiting GLS1, the first and rate-limiting step of glutaminolysis, reportedly prevents the activation of hepatic stellate cells and halts fibrosis progression in preclinical murine models induced with carbon tetrachloride (CCl_4) or methionine and choline deficient (MCD) diet[5]. Additionally, scavenging ammonia, a toxic byproduct of glutaminolysis, reportedly plays a crucial role against the development or progression of liver fibrosis[15]. Therefore, targeting glutamine metabolic processes presents an attractive and feasible strategy for the treatment of NASH.

The development of small-molecule inhibitors, such as bis-2-(5-phenylacetamido-1,3,4-thiadiazol-2-yl)ethyl sulfide (BPTES)[16], CB-839[17], and Compound 968[18] has paved new avenues for metabolism-targeted therapies that modulate GLS1 activity to regulate glutaminolysis. However, it is important to acknowledge the potential concerns associated with the use of the metabolic therapies in the management of NASH, because of a lack of understanding of metabolic adaptation and reprogramming in living bodies during interventions targeting glutaminolysis. Functional positron emission tomography (PET) imaging is a potentially ideal tool for capturing real-time variations of glutaminolysis in NASH, especially following GLS1 intervention in a therapeutic setting. It offers non-invasive, highly sensitive, repetitive, and quantitative imaging using positron-emitting probes that specifically target the metabolic processes of interest. A notable example of PET imaging regarding metabolism is the assessment of glucose uptake using 2-[^{18}F]fluoro-2-deoxy-d-glucose ([^{18}F]FDG), a ^{18}F-labelled glucose analogue. PET imaging with [^{18}F]FDG is routinely used in clinical settings worldwide to evaluate glucose uptake as a surrogate for the Warburg effect in cancer diagnosis, staging, and monitoring[19,20]. The use of glutamine-based PET imaging to study the relationship between glutaminolysis dynamics and metabolic therapy in NASH has never been reported, despite several glutamine analogues being radiolabelled for use in pharmacokinetic studies and cancer imaging[21–24].

Given the crucial role of glutaminolysis in various processes of NASH, we envisioned that L-glutamine-based PET has significant potential as an effective imaging platform for gaining valuable insights into whole-body glutamine metabolism. This could guide the development of clinically relevant therapeutic interventions using potent metabolic modulators for the treatment of NASH. To test this hypothesis, we utilised a ^{11}C-labelled L-glutamine (L-[5-^{11}C]glutamine, [^{11}C]Gln, Fig. 1A) PET probe[22] to investigate the global pharmacokinetics of L-glutamine and its relationship with glutaminolysis and therapeutic response under both healthy and disease conditions, as well as following single and systemic administration of a uncompetitive GLS1 inhibitor, BPTES[16]. In advance, we developed a simple and rapid method for synthesizing [^{11}C]Gln, which can be easily automated and translated for clinical use[25]. Specifically, we focused on the construction of an imaging platform with [^{11}C]Gln PET and verified its use in NASH, particularly in the context of treatment with BPTES. This study aimed to demonstrate that [^{11}C]Gln PET can serve as a valuable imaging platform for assessing glutamine metabolism in whole-body and real-time settings. By doing so, we sought to provide comprehensive insights into the reprogrammed metabolic responses associated with NASH and glutaminolysis-based metabolic intervention.

2. Materials and methods

2.1. Radiosynthesis of [^{11}C]Gln

[^{11}C]Gln was synthesized using hydrogen [^{11}C]cyanide ([^{11}C]HCN) as a labelling agent, equipped with a fully automated synthesis system developed in-house[26]. [^{11}C]CO_2 was generated under a cyclotron (CYPRIS HM-18; Sumitomo Heavy Industries, Tokyo, Japan), and was then passed through a nickel wire tube to obtain a mixture of [^{11}C]methane ([^{11}C]CH_4) in carrier gas. The resulted [^{11}C]CH_4 was mixed with NH_3 gas and passed through a heated platinum furnace at 950 °C to produce [^{11}C]HCN.

During the production of [^{11}C]HCN, a mixture of 18-crown-6 (8 mg in 900 μL of CH_3CN) and Cs_2CO_3 (3 mg in 150 μL of water) was azeotropically dried and then added to CH_3CN

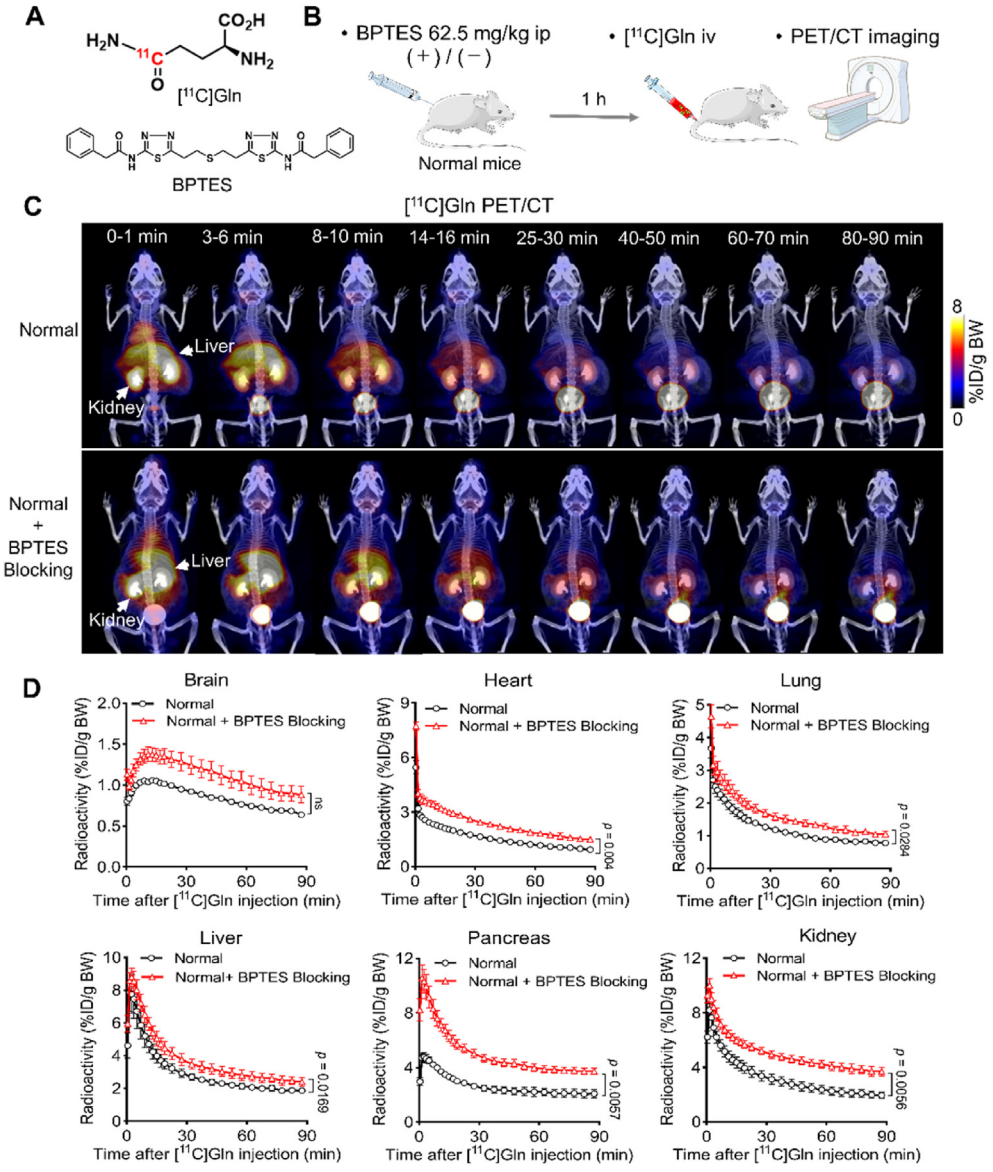

Figure 1 PET imaging with [^{11}C]Gln visualizes and quantifies the global behaviours of L-glutamine under healthy conditions and subsequent to GLS1 intervention. (A) Chemical structures of [^{11}C]Gln and BPTES. (B) The [^{11}C]Gln PET imaging protocol under healthy conditions and subsequent to GLS1 intervention. (C) Representative three-dimensional pharmacokinetic images of [^{11}C]Gln PET/CT at different time points post-injection, with or without BPTES intervention. A single administration study was conducted on normal mice by administrating excess BPTES (62.5 mg/kg) 1 h before [^{11}C]Gln injection ($n = 4$). (D) Time−activity curves (TACs) of [^{11}C]Gln in the brain, heart, lungs, liver, pancreas, and kidneys. Data are expressed as the mean percentage of the injected radioactivity dose per gram of body weight (%ID/g BW) ± SEM ($n = 4$). Radioactivity comparisons at 90 min after [^{11}C]Gln injection were performed using an unpaired two-tailed Student's t test.

(300 μL). The automatically produced [^{11}C]HCN was trapped into the CH_3CN solution to yield [^{11}C]CsCN. Precursor **1** (3.5 mg) in CH_3CN (300 μL) was added the [^{11}C]CsCN solution and the reaction mixture was heated at 90 °C for 8 min, followed by complete removal of the reaction solvent. After the [^{11}C]cyanation, CF_3COOH (TFA) and H_2SO_4 (4:1, 500 μL) was added to the residue and this reaction mixture was heated at 80 °C for 5 min. After the reaction, the mixture was diluted with diethyl ether (1.5 mL) and passed through a silica plus Sep-Pak cartridge to trap [^{11}C]Gln. The cartridge was washed with diethyl ether (10 mL) and then eluted with phosphate buffer (5 mL). The [^{11}C]Gln solution was obtained by removal of diethyl ether from the eluant, followed by addition of phosphate buffer (4 mL) for use.

2.2. *Studies in mice, mouse models, ethics statements and drug treatment*

Animal experiments were conducted on 6−8-week-old male C57BL/6 mice (body weight, 23.1 ± 0.24 g) (Japan SLC, Shizuoka, Japan). All the animal procedures were approved by the Animal Ethics Committee of National Institutes for Quantum Science and Technology (QST, approval number: 16-1005 and 16-1006). The mice were housed and handled under specific pathogen-free conditions, including a 12-h light/dark cycle, 50% relative humidity, and temperatures between 25 and 27 °C. They had free access to tap water and were fed either a chow diet (as a control) or a MCD diet (Cat# 518810, Dyets, Bethlehem, PA, USA) for 8 weeks. During

the latter half of a 4-week period, the MCD diet-fed mice were randomized to receive intraperitoneal injections of BPTES (12.5 mg/kg, Cat#SML0601, Sigma−Aldrich, St. Louis, MO, USA) three times a week[3], forming the BPTES treated group. A separate group of MCD diet-fed mice served as the NASH untreated group and received injections without BPTES. A single administration study was conducted on both normal mice and NASH mice by injecting excess BPTES (62.5 mg/kg) at 1 h before [^{11}C]Gln injection, creating the BPTES blocking group. This administration schedule adhered to the recommendations of the National Institute of Health and the institutional guidelines of the QST. All experiments were carried out as unblinded studies. Mice were fasted overnight with free access to water, and radioactivity uptake experiments were conducted at least 48 h after the last treatment administration. All *in vitro* experiments were conducted in triplicates (technical replicates) and repeated independently at least three times unless otherwise noted. The end point of *in vivo* experiments was set at 8 weeks after implementing specific diets.

2.3. Dynamic PET/computed tomography (CT) and PET data analysis

PET scans were performed using a small-animal Inveon PET scanner (Siemens, Knoxville, TN, USA) after intravenous injection of [^{11}C]Gln (9.22−10.26 MBq/0.3 mL). The scanner provided 159 transaxial slices with 0.796 mm (centre-to-centre) spacing, a 10 cm transaxial field of view (FOV), and a 12.7 cm axial FOV. Emission scans were acquired in the three-dimensional list mode with an energy window of 350−650 keV under isoflurane anesthesia. Scans were performed from 0 to 90 min in normal mice and from 0 to 30 min in MCD diet-fed mice after [^{11}C]Gln injection. All list-mode acquisition data were sorted into three-dimensional sinograms, which underwent Fourier rebinning into two-dimensional sonograms. Corrections were applied for scanner dead time, randoms, and decay of the injected radioprobe. The dynamic images were reconstructed using filtered back-projection with a Hanning's filter and a Nyquist cutoff of 0.5 cycles/pixel. Immediately after the PET scans, contrast-enhanced CT scans were performed in the normal mice by injecting 0.4 mL of non-ionic contrast medium (Iopamiron 370, Bayer, Osaka, Japan) for 34 s, with the purpose of assisting in the segmentation of organs. Non-enhanced scans with the breath-holding model in MCD diet-fed mice were performed for 4 min. The scan conditions included radiation parameters of 200 μA, 90 kV, and a FOV of 60 mm using a small-animal CT system (R_mCT2; Rigaku, Tokyo, Japan). Averaged CT attenuation and dynamic PET images were reconstructed and fused using Siemens Inveon Research Workplace (IRW) software (version 4.0).

Regions of interest (ROIs) in major organs and tissues were manually outlined in the PET/CT fusion images using IRW 4.0. The average radioactivity concentration was calculated using the mean pixel values in the ROI. The regional uptake of radioactivity was decay-corrected to the injection time, normalised to body weight, and expressed as a percentage of the injected dose per gram of body weight (%ID/g BW). Time−activity curves (TACs) of [^{11}C]Gln in individual organs and tissues were determined. The hepatic radioactivity values in each group of mice were compared at 25−30 min post-injection.

2.4. Ex vivo biodistribution studies

The mice were sacrificed by cervical dislocation at specific time points after [^{11}C]Gln (1.70−1.85 MBq/0.1 mL, corresponding to 6.70−7.29 ng of L-Gln) injection. The major organs and tissues, including blood, heart, lungs, liver, pancreas, spleen, kidneys, intestines, muscle, and brain, were promptly removed, collected, and weighed. The radioactivity in each tissue sample was measured using a 2480 Wizard auto-γ scintillation counter (PerkinElmer, Waltham, MA, USA), and expressed as a percentage of the injected dose per gram of wet tissue weight (%ID/g tissue weight). All radioactivity measurements were corrected for decay.

2.5. Histopathology

After completion of the PET and CT scans, the mice were euthanised *via* cervical dislocation. The livers were harvested and weighed on a microscale, fixed in 10% formalin, embedded in paraffin, and sectioned into 5 μm slices. The liver sections were stained with hematoxylin and eosin (H&E; Muto Pure Chemical, Tokyo, Japan) and masson's Trichrome (MT; Sigma−Aldrich), following the manufacturer's instructions. The histopathological assessment was scored in a blinded manner by three pathologists using the non-alcoholic fatty liver disease activity score (NAS) system (Supporting Information Table S1)[27]. Additionally, the liver tissue sections were deparaffinised in xylene and gradually rehydrated using graded alcohol. The tissue sections were then incubated overnight at 4 °C with a primary antibody rabbit anti-GLS1 antibody (1:100; Cat#12855-1-AP, Proteintech, Rosemont, IL, USA). The slides were then incubated with the secondary antibody Alexa Fluor® 488 goat anti-rabbit IgG (1:500; Cat#A27034, Invitrogen, Carlsbad, CA, USA), for 60 min at room temperature. Finally, the slides were mounted using a mounting medium containing with DAPI (Cat#H-1200, VectorLabs, Newark, CA, USA). Images were captured using a Keyence BZ-X710 microscope (Keyence, Osaka, Japan). The frequency of positively stained areas was quantified automatically using a specialized Hybrid Cell Count software (Keyence). The results are presented as the percentage of the total tissue area showing positive staining. Negative control slides were processed without the primary antibody, secondary antibody, or with an isotype control IgG to ensure specificity.

2.6. RNA preparation and quantitative real-time polymerase chain reaction (qRT-PCR) analysis

The liver samples were flash-frozen in liquid nitrogen immediately after surgical removal and macro dissected prior to RNA extraction. Total RNA was extracted using the RNeasy Mini Kit (Qiagen, Valencia, CA, USA), following the manufacturer's instructions. The quality of the total RNA was measured using the 260/280 nm ratio with NanoDrop 2000 (Thermo Scientific, Wilmington, DE, USA). For qRT-PCR, a TaqMan system was employed on an Applied Biosystems StepOne™ machine (Carlsbad, CA, USA), according to the manufacturer's instructions. Target-specific primers and probes for mouse *GLS1* (Mm01257297_m1), tumor necrosis factor-alpha (*TNF-α*, Mm00443258_m1), interleukin-17 (*IL-17*, Mm00439618_m1), *GLS2* (Mm01164862_m1), and 18S *ribosomal RNA* (18S rRNA, *Hs99999901_s1*) were purchased from Applied Biosystems. The normalised cycle threshold (C_t) value for each gene was determined by subtracting the C_t value obtained for 18S rRNA. The fold change in the mRNA levels of each gene compared to the corresponding control levels was calculated.

2.7. *Quantification and statistical analysis*

Quantitative data are reported as mean ± standard error of the mean (SEM). Intergroup comparisons were conducted using either an unpaired two-tailed Student's *t*-test or a one-way analysis of variance (ANOVA) followed by Tukey's multiple comparison test. Prism version 8.3 software (GraphPad Software, La Jolla, CA, USA) was used for statistical analyses. Pearson's correlation analysis was used to estimate the relationship between hepatic radioactivity, and GLS1 expression or NAS. The threshold for statistical significance was set at $P < 0.05$.

3. Results

3.1. *Radiosynthesis of [^{11}C]Gln*

[^{11}C]Gln was synthesized by [^{11}C]cyanation of an iodine precursor (**1**) with [^{11}C]CsCN, followed by hydrolysis and deprotection of the radioactive intermediate [^{11}C]**2** with TFA and H_2SO_4, using an automated multi-purpose radiosynthesis apparatus (Scheme 1). In the previous procedures, the intermediate [^{11}C]**2** was purified by solid phase extraction or semi-preparative HPLC purification[22,28,29]. In our study, [^{11}C]**2** was not separated and the reaction mixture of [^{11}C]cyanation was directly treated with TFA and H_2SO_4 to undergo hydrolysis and deprotection. Solid phase extraction for the final reaction mixture produced the [^{11}C]Gln injection. Compared with the previous procedures, our present protocol shortened the production time and simplified the procedures of [^{11}C]Gln.

Starting from 37 GBq of [^{11}C]CO_2, 2.3−4.4 GBq ($n = 20$) of [^{11}C]Gln was produced at EOS. The average synthesis time was 33 min from the end of bombardment (EOB). The molar activity and radiochemical purity of [^{11}C]Gln in the final product solution were 70−120 GBq/μmol and >90%, respectively. Moreover, the enantiomeric purity of [^{11}C]Gln exceeded 95% enantiomeric excess at EOS. These analytical results were in compliance with our in-house quality control/assurance specifications.

3.2. *PET imaging with [^{11}C]Gln visualizes and quantifies the whole-body behaviours of l-glutamine under healthy conditions and subsequent to GLS1 intervention*

To investigate the whole-body pharmacokinetics of L-glutamine and its response following GLS1 interventions under healthy conditions, we conducted dynamic PET/CT scans in normal mice from 0 to 90 min after radioinjection for the baseline. Furthermore, PET scans were obtained within 1 h after a single administration of BPTES (62.5 mg/kg) preceding [^{11}C]Gln injection (Fig. 1A and B). This dosage was 5 times higher than the treatment dose employed in previous experiments with NASH mouse models[3]. Fig. 1C and Supporting Information Movie 1 present typical global pharmacokinetic images of [^{11}C]Gln. A rapid concentration of [^{11}C]Gln was seen in the kidneys during 0−16 min post-injection, followed by concentrated renal medulla and urine under baseline conditions (Fig. 1C upper). The liver showed moderate radioactivity during 10 min post-injection, followed by rapid washout. Administration of a single dose of the GLS1 inhibitor BPTES slowed down the washout rate in the kidneys and liver compared to baseline (Fig. 1C down), leading to higher signal of [^{11}C]Gln under acute blocking conditions in normal mice. The bladder showed the highest signal, correlating with the excretion of the radiotracer under both conditions.

Supporting video related to this article can be found at https://doi.org/10.1016/j.apsb.2024.07.023.

The temporal distribution of L-glutamine in individual organs and tissues was quantified using dynamic [^{11}C]Gln PET scans. Fig. 1D depicted the TACs of [^{11}C]Gln both at baseline and following GLS1 blocking with BPTES. The quantified results showed that the administration of the GLS1 inhibitor BPTES induced a significantly increased accumulation of [^{11}C]Gln compared to baseline in the main organs of normal mice, including the heart, lungs, liver, pancreas, and kidneys, within 90 min after [^{11}C]Gln injection. This increase was presumably due to acute inhibition of GLS1 activity by BPTES, forming an inactive tetramer, as describe[30,31], consequently inhibiting glutaminolysis. In contrast, BPTES exposure yielded similar TACs of [^{11}C]Gln in the brain under both conditions, remaining stable and at a low level throughout the dynamic scan. These results suggest that utilizing PET imaging with [^{11}C]Gln enables the visualization and quantification of the *in vivo* behaviors of L-glutamine, as well as the metabolic responses of glutaminolysis to GLS1 intervention under healthy conditions, in a temporal-spatial pattern.

3.3. *[^{11}C]Gln provides direct evidence of accumulation in each organ and tissue*

To further explore the behavior of L-glutamine, we measured the distribution of [^{11}C]Gln in the major organs and tissues at specific time points after injection (Fig. 2A). Fig. 2B depicted the

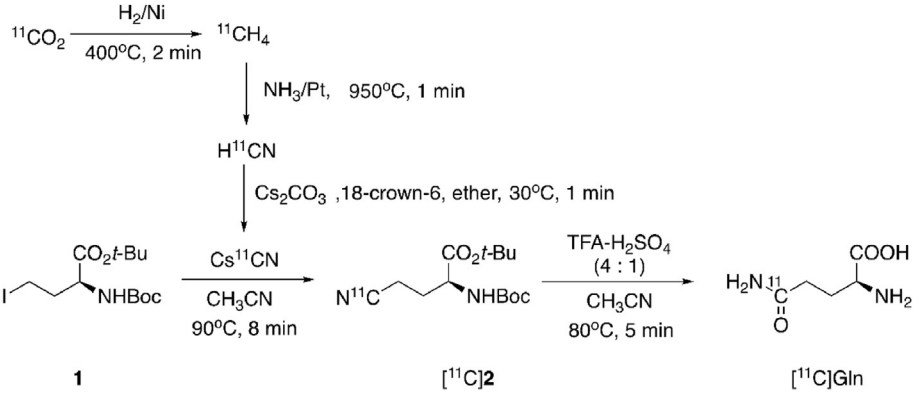

Scheme 1 Radiosynthesis of L-[5-^{11}C]glutamine ([^{11}C]Gln).

biodistribution of L-glutamine *in vivo*. In normal physiology, high radioactivity of [^{11}C]Gln was verified in the main organs, including the blood, heart, lung, pancreas, and kidney during the initial 1 min after [^{11}C]Gln injection. Over time, blood levels of [^{11}C]Gln decreased rapidly, resulting in low blood activity at 60 min after injection. The liver exhibited a peak activity at 5 min, followed by a washout, whereas uptake in the pancreas increased up to 5 min and then reached a high plateau, as expected for a radiolabeled amino acid[23]. Rapid uptake was observed in the kidneys, with quickly excreted through the bladder. Brain uptake exhibited a relatively low level, with slow washout throughout the 60 min experiment. The *ex vivo* biodistribution analysis confirmed the findings of the pharmacokinetic PET/CT images, and provided direct evidence of [^{11}C]Gln accumulation in each organ and tissue.

3.4. *GLS1 intervention metabolic therapy ameliorates NASH*

A radiolabelled L-glutamine probe could noninvasively and quantitatively track dynamic glutaminolysis, providing insights into the metabolic responses to GLS1-blockade therapy. To test this hypothesis, we first established a metabolic therapeutic model in NASH mice using intraperitoneal injections of the GLS1 inhibitor BPTES (12.5 mg/kg) three times per week for the latter half of a 4-week period (Fig. 3A). The selection of the MCD diet model, dose preparation and administration, and treatment duration were determined based on previous experiments[3,32–34]. These studies had identified abnormal glutamine catabolism and increased GLS1 presence in hepatic biopsies of NASH patients and MCD diet-fed preclinical murine models for NASH[3,4]. Our MCD fed mice exhibited increased hepatic GLS1 levels compared to those fed a chow diet (Fig. 3B–D). Treatment with BPTES resulted in lower GLS1 expression, at both protein (Fig. 3B and C) and mRNA levels (Fig. 3D). Under these conditions, GLS2, typically distributed around the hepatic periportal compartment, was found to be decreased in the livers of untreated and BPTES treated NASH mice (Supporting Information Fig. S1). These findings are consistent with the results reported in previous studies[3,4].

The mice subjected to the MCD diet for 8 weeks showed significant weight loss, increased liver weight, and a higher ratio of liver to body weight than those fed the chow diet (Fig. 3E–G), consistent with the finding of previous reports[32,33]. Notably, BPTES treatment did not cause any differences in body weight (Fig. 3E), liver weight (Fig. 3F), or the ratio of liver to body weight (Fig. 3G) in the MCD diet-fed mice. However, BPTES treatment did lead to a significantly decreased level of mRNA of hepatic pro-inflammatory cytokines, such as *TNF-α* (Fig. 3H) and *IL-17* (Fig. 3I). TNF-α is an adipokine known to promote inflammation, insulin resistance, hepatocyte injury, and fibrosis[35], while IL-17 is implicated in the progression of nonalcoholic fatty liver disease[36]. To assess liver injury and fibrosis, H&E and MT staining were performed and evaluated using the NAS system (Table S1)[27]. Using the NAS template, we observed that MCD diet-fed mice displayed several NASH-associated pathologies, while the pharmacological inhibition of GLS1 using BPTES effectively reduced the severity of these pathological findings (Fig. 3J and Table 1). Untreated MCD diet-fed mice had a NAS of 9.25 ± 0.16, while BPTES-treated MCD diet-fed mice exhibited a significantly lower NAS of 2.41 ± 0.37. These findings highlight the improvement in liver damage achieved through GLS1-blockade metabolic therapy with BPTES, thereby validating the use of BPTES-treated MCD diet-fed mice as an appropriate preclinical mouse model for investigating glutamine metabolism and assessing therapeutic efficacy after GLS1 intervention in the context of NASH.

3.5. *[^{11}C]Gln PET provides an imaging platform for tracking glutaminolysis in NASH and following GLS1 intervention therapy*

To test our hypothesis, we performed whole-body dynamic PET/CT imaging in mice subjected to the MCD diet to simulate NASH conditions and investigated the imaging alterations resulting from systemic therapeutic interventions with BPTES, from 0 to 30 min after injection of [^{11}C]Gln (Fig. 4A). Furthermore, to assess the direct impact of GLS1 intervention on hepatic [^{11}C]Gln imaging, we performed a single administration study by pre-injecting an excess of BPTES (62.5 mg/kg) at 1 h in untreated NASH mice. Fig. 4B shows representative co-registered [^{11}C]Gln PET/CT images captured between 25 and 30 min after injection. This imaging timeframe was selected based on pharmacokinetic images of [^{11}C]Gln in normal mice, indicating that uptake of [^{11}C]Gln in livers remained at relatively stable levels after 20 min post-injection (Fig. 1C and D). In contrast to the pharmacokinetics of [^{11}C]Gln under healthy conditions, PET/CT imaging with [^{11}C]Gln revealed a significantly higher hepatic uptake in mice fed the MCD diet compared to those fed the chow diet. Interestingly, the heightened uptake exhibited minimal impact following a single GLS1 intervention with BPTES administration (Fig. 4B), suggesting glutamine metabolic adaptation and reprogramming in the context of NASH[3]. Notably, systemic metabolic therapy with BPTES reduced the hepatic avidity of [^{11}C]Gln in the MCD diet-fed mice (Fig. 4B), aligning with the lower GLS1 expression observed in the treated NASH mice (Fig. 3B–D).

We also quantified the TACs of [^{11}C]Gln in the livers (Fig. 4C) based on dynamic PET and corresponding CT images taken from

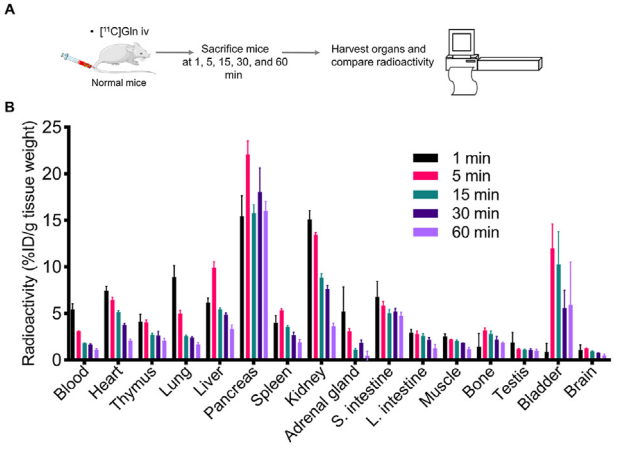

Figure 2 [^{11}C]Gln provides direct evidence of accumulation in each organ and tissue. (A) The *ex vivo* biodistribution protocol under healthy conditions. (B) Quantitative measurement of radioactivity in the main organs and tissues following *ex vivo* biodistribution analysis at 1, 5, 15, 30, and 60 min after [^{11}C]Gln injection; $n = 3$ for each time point. Data are expressed as the mean percentage of the injected radioactivity dose per gram of tissue weight (%ID/g tissue weight) ± SEM. All comparisons were performed using an unpaired two-tailed Student's *t* test. S. intestine, small intestine; L. intestine, large intestine.

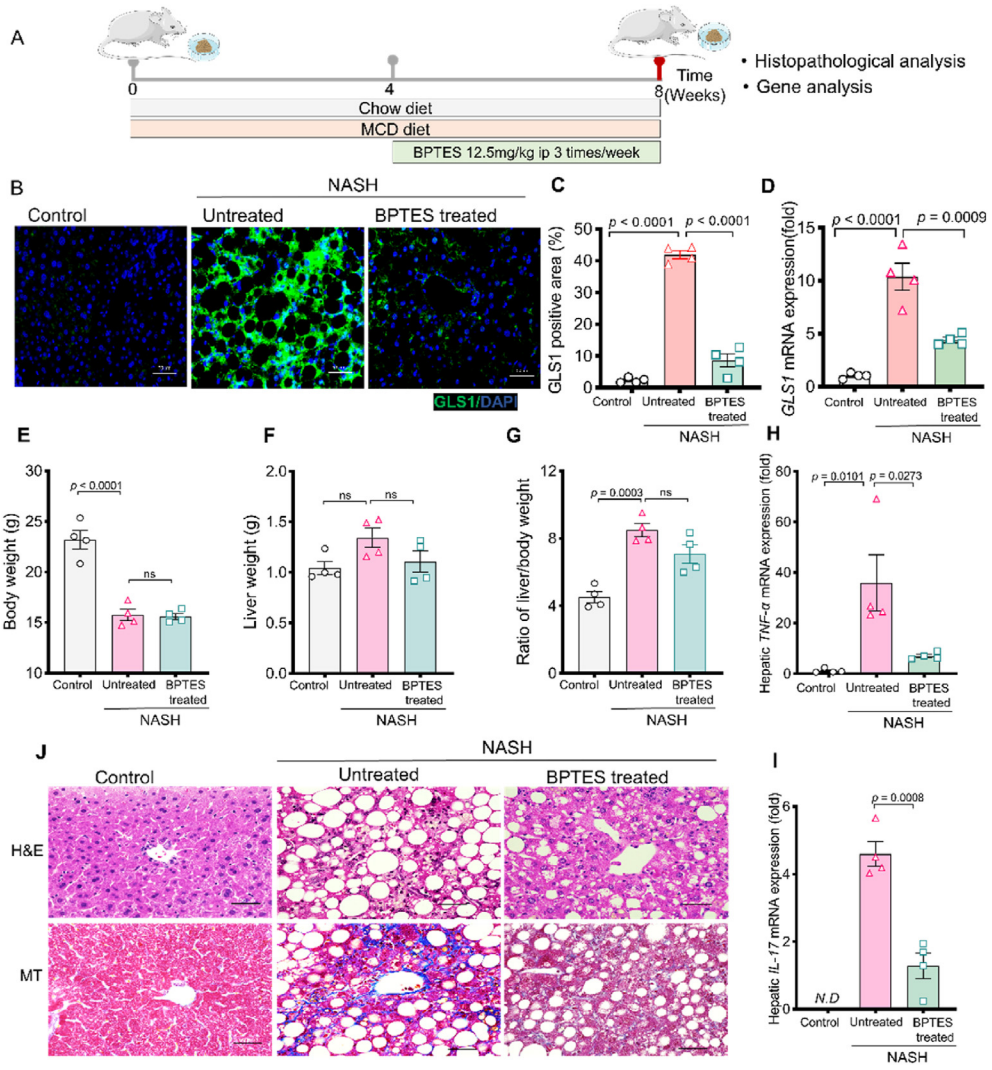

Figure 3 GLS1-blockade metabolic therapy with BPTES ameliorates NASH. (A) Schematic representation of the experimental design in the murine NASH model. (B) Representative fluorescence images of hepatic GLS1 (green), and DAPI (blue) performed on paraffin sections from MCD diet-fed mice systemic treated either with or without BPTES. Scale bar: 50 µm. Representative images are obtained from three independent experiments, stained using a primary rabbit anti-GLS1 antibody (1:100; Cat#12855-1-AP, Proteintech), followed by incubation with the secondary antibody Alexa Fluor® 488 goat anti-rabbit IgG (1:500; Cat#A27034, Invitrogen). (C) Hepatic GLS1 expression quantified by immunohistochemistry. (D) Quantification of hepatic *GLS1* using qRT-PCR. (E) Body weight. (F) Liver weight. (G) Ratio of the liver to body weight. (H, I) Quantification of hepatic *TNF-α* and *IL-17* using qRT-PCR. (J) Representative pathological images of H&E and MT staining of the livers. Scale bar: 50 µm. Representative images are shown from three independent experiments. Data are presented as mean ± SEM, $n = 4$ for each group. All comparisons were performed using one-way ANOVA followed by Tukey's multiple comparison test. H&E, hematoxylin-eosin; MT, Masson's trichome; NASH, non-alcoholic steatohepatitis.

Table 1 The histopathological scoring of mice fed a MCD diet, with or without systemic therapeutic interventions with BPTES.

Histopathological feature	Control	NASH	
		Untreated	BPTES treated
Steatosis	0.00 ± 0.00	2.75 ± 0.08	1.00 ± 0.00**
Ballooning	0.00 ± 0.00	1.58 ± 0.08	0.33 ± 0.14**
Inflammation	0.00 ± 0.00	2.58 ± 0.24	0.50 ± 0.29**
Fibrosis	0.00 ± 0.00	2.33 ± 0.14	0.58 ± 0.25**
Total NAS	0.00 ± 0.00	9.25 ± 0.16	2.41 ± 0.37**

The data are expressed as the mean ± SEM; $n = 4$ for each group. All comparisons between untreated and BPTES treated NASH mice were performed using unpaired two-tailed Student's *t*-test. **$P < 0.01$. NASH, non-alcoholic steatohepatitis; BPTES, bis-2-(5-phenylacetamido-1,3,4-thiadiazol-2-yl)ethyl sulfide; NAS: non-alcoholic fatty liver disease activity score.

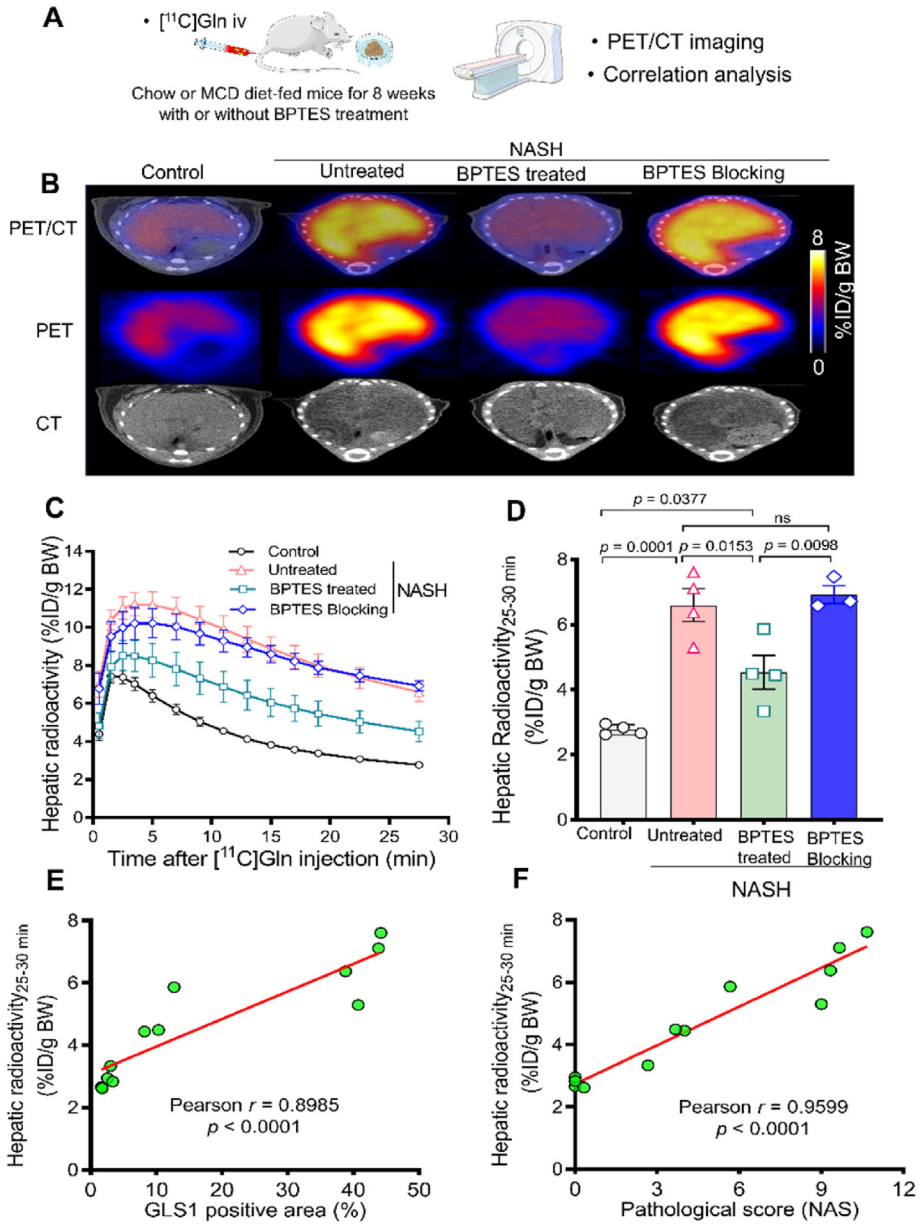

Figure 4 [^{11}C]Gln PET provides an imaging platform for tracking glutaminolysis in NASH and following GLS1 intervention therapy. (A) Schematic representation of the imaging experimental design in the murine NASH model. (B) Representative hepatic PET/CT images in mice fed a MCD diet, with or without systemic therapeutic interventions with BPTES (n = 4). A single administration study was conducted on untreated NASH mice by administrating excess BPTES (62.5 mg/kg) 1 h before [^{11}C]Gln injection (n = 3). The PET images were summed from 25 to 30 min after [^{11}C]Gln injection. Each PET/CT image is representative of at least three independent experiments. (C) Time−activity curves showing the dynamics of [^{11}C]Gln in the livers of all groups of mice (n = 3−4). (D) Hepatic radioactivity$_{25-30\ min}$ value of PET with [^{11}C]Gln (n = 3−4). (E) Pearson correlation analysis of radioactivity and GLS1 protein expression within the livers, including samples from control, untreated NASH, and BPTES treated NASH mice (n = 4 in each group). (F) Pearson correlation analysis of radioactivity and NAS within the livers, including samples from control, untreated NASH, and BPTES treated NASH mice (n = 4 in each group). Data are expressed as the mean percentage of the injected radioactivity dose per gram of body weight (%ID/g BW) ± SEM (n = 3−4). All comparisons were performed using one-way ANOVA followed by Tukey's multiple comparison test.

0 to 30 min after the injection. The tracer uptake in the livers of MCD diet-fed untreated mice, quantified as hepatic radioactivity at 25−30 min, was significantly higher than that of the control group and the BPTES-treated MCD diet-fed group (Fig. 4D). Similar to the tumor cell trapping of [^{18}F]FDG through upregulation of membrane-bound glucose transporter 1 and cytosolic hexokinase[37], we propose that the heightened expression of GLS1 in the NASH liver could lead to increased [^{11}C]Gln uptake. The results also support the notion that glutamine metabolism is reprogrammed under NASH conditions, suggesting the role of BPTES in the NASH treatment process beyond a simple inhibitor-response relationship[3,4]. The correlation analysis revealed that

there was indeed a strong correlation between hepatic radioactivity and GLS1 protein expression (Fig. 4E; Pearson's $r = 0.8985$, $P < 0.0001$), as well as between the hepatic radioactivity and NAS (Fig. 4F; Pearson's $r = 0.9599$, $P < 0.0001$). These findings demonstrate that [^{11}C]Gln PET imaging can capture reprogrammed changes in glutamine metabolism under NASH conditions and during metabolic therapy targeting GLS1, potentially identifying the therapeutic efficacy of manipulating glutaminolysis with the GLS1 inhibitor in a living body.

4. Discussion

Targeting glutamine metabolism has shown promising results in the treatment of liver related diseases. Recent clinical studies have aimed to identify effective methods for understanding metabolic responses, determining metabolic status, and predicting therapeutic efficacy in a living body during interventions targeting glutaminolysis[38–40]. Quantitative PET imaging is an ideal tool for these purposes. In this study, we utilised [^{11}C]Gln to monitor the whole-body pharmacokinetics of l-glutamine and its alterations following GLS1 interventions under healthy conditions. [^{11}C]Gln PET captured the temporal-spatial pattern of distribution and action of L-glutamine, as well as the dynamic responses after a single administration of BPTES, a GLS1 inhibitor, within the body. Furthermore, we tracked the metabolic response of glutaminolysis in mice with NASH and during therapy with BPTES. [^{11}C]Gln PET imaging revealed a significant increase in hepatic uptake in NASH mice fed the MCD diet, which was minimally disrupted by a single BPTES administration under the specific disease conditions. However, systemic metabolic therapy with BPTES reduced the hepatic avidity of [^{11}C]Gln in MCD diet-fed mice. This reduction in [^{11}C]Gln uptake correlated with a decrease in the GLS1 burden and improvements in liver damage, suggesting the therapeutic efficacy of BPTES in mitigating NASH-related metabolic abnormalities. Our study highlights the potential of [^{11}C]Gln PET imaging as an unprecedented imaging platform for noninvasively tracking reprogrammed metabolic responses in NASH and during therapeutic interventions targeting glutaminolysis, as well as for evaluating the therapeutic efficacy of GLS1-tageting metabolic manipulation in a living body.

In-depth investigations regarding the role of glutaminolysis in liver related diseases may be crucial for understanding the metabolic plasticity of NASH and developing metabolic therapeutic strategies. Using various radiotracers, PET imaging has become a crucial tool for assessing *in vivo* metabolism and has extensive clinical implications[19,23,41]. Glutamine analogues labelled with radionuclides such as ^{18}F or ^{11}C, including (2*S*,4*R*)-4-[^{18}F]fluoroglutamine, [^{18}F](2*S*,4*S*)-4-(3-fluoropropyl)glutamine and [^{11}C]Gln, have been utilised in preclinical and clinical studies to investigate various cancers[22,42–44]. These radiotracers specifically provide tumour metabolic imaging information, particularly regarding the l-glutamine uptake relevant to tumour pathology. Recently, we developed a simple and rapid method for synthesising [^{11}C]Gln[25]. In this study, we demonstrated its utility as a metabolic imaging agent in the NASH. These advancements may facilitate the future use of [^{11}C]Gln and provide critical tools for understanding *in vivo* dysfunctional glutamine metabolism and its relationship with liver diseases.

GLS1 expression is up-regulated in various cell types in response to liver diseases, and depleting GLS1 improves liver function[3,4,6]. Our findings agree with those of the aforementioned studies, as we observed elevated expression of GLS1 in the livers of NASH mice, accompanied by increased levels of pro-inflammatory cytokines TNF-α and IL-17. Inhibition of GLS1 with BPTES effectively mitigated NASH-associated pathologies, including hepatic steatosis, inflammation, and fibrosis, consistent with previous reports[4,5]. We also used [^{11}C]Gln PET imaging to track the dynamic response of glutaminolysis in NASH mice treated with BPTES. We found a significant positive correlation between the hepatic uptake of [^{11}C]Gln and GLS1 expression, as well as the NAS. Our proposal is that heightened GLS1 expression enhances the conversion of L-glutamine to glutamate, leading to a compensatory increase in [^{11}C]Gln uptake to meet elevated metabolic demands. This mechanism is analogous to what is observed in tumor cells with [^{18}F]FDG uptake, facilitated by the upregulation of membrane-bound glucose transporter 1 and cytosolic hexokinase. Similarly, the increased expression of GLS1 in the NASH liver may enhance L-glutamine uptake, leading to the amplified accumulation of labeled L-glutamine probes [^{11}C]Gln within liver cells, enabling their visualization through PET imaging. These results highlight the potential of [^{11}C]Gln PET imaging as a platform for identifying metabolic responses and therapeutic efficacy during interventions targeting GLS1 in NASH and liver diseases. GLS1 inhibitors, including UPGL00004[45], compound 968[18], BPTES[16], CB-839[17], and IACS-6274[46], are promising metabolic drugs for treating various cancers. Notably, IACS-6274[47] is currently undergoing phase I clinical trials (NCT05039801), and CB-839[48] has completed phase II clinical trials (NCT03163667). However, it is important to carefully consider the potential effects of strategies that affect whole-body glutamine metabolism. The [^{11}C]Gln PET imaging platform, which enables the visualization and quantification of glutaminolysis dynamics in a living body, can provide valuable insights into how glutamine metabolism changes with NASH and its contribution to the disease process, facilitating the development of GLS1 inhibitors and novel metabolic therapeutic strategies targeting NASH-related conditions, both in clinical and research settings.

This study has some limitations. First, we utilized the [^{11}C]Gln PET imaging platform in animal models of NASH induced by a MCD diet, in which NASH developed rapidly within 8 weeks of dietary intervention. It would be essential to validate these findings in other models of NASH, particularly chronic pre-clinical models that closely resemble the progressive nature of human pathology, such as the novel Amylin liver NASH model. Additionally, studying the efficacy of various GLS1 inhibitors in these models and other age-related diseases would provide a more comprehensive understanding of the clinical value of this imaging approach. Following this proof-of-concept study, further investigations are underway to explore the potential clinical applications of [^{11}C]Gln PET imaging.

5. Conclusions

In summary, our study successfully constructed a [^{11}C]Gln imaging platform and demonstrated its utility in monitoring the whole-body pharmacokinetics of L-glutamine under both healthy and NASH disease conditions. Furthermore, we tracked the dynamic responses of glutaminolysis in NASH mice during metabolic therapy with BPTES using [^{11}C]Gln PET imaging. Our findings highlight the potential of [^{11}C]Gln PET as a valuable tool for identifying and studying the metabolic responses and therapeutic efficacy during interventions targeting glutaminolysis.

Acknowledgments

This work was supported in part by the Moonshot Research and Development Program (Grant No. 21zf0127003h001, Japan), JSPS A3 Foresight Program (Grant No. JPJSA3F20230001, Japan), and JSPS KAKENHI (Grants No. 23H02867, 23H05487, and 21K07659, Japan). We would like to thank the staff of National Institute for Quantum Science and Technology for their technical support in the radiosynthesis and animal experiments.

Author contributions

Yiding Zhang: Writing − review & editing, Writing − original draft, Visualization, Validation, Project administration, Methodology, Formal analysis, Conceptualization. Lin Xie: Writing − review & editing, Writing − original draft, Visualization, Validation, Supervision, Project administration, Methodology, Investigation, Funding acquisition, Formal analysis, Data curation, Conceptualization. Masayuki Fujinaga: Writing − review & editing, Validation, Project administration, Methodology, Formal analysis. Yusuke Kurihara: Writing − review & editing, Visualization, Project administration, Methodology. Masanao Ogawa: Writing − review & editing, Visualization, Project administration, Data curation. Katsushi Kumata: Writing − review & editing, Validation, Project administration, Methodology. Wakana Mori: Writing − review & editing, Project administration, Methodology. Tomomi Kokufuta: Writing − review & editing, Visualization, Project administration, Methodology. Nobuki Nengaki: Writing − review & editing, Visualization, Project administration, Methodology. Hidekatsu Wakizaka: Writing − review & editing, Project administration, Methodology. Rui Luo: Writing − review & editing, Project administration, Methodology, Investigation. Feng Wang: Writing − review & editing, Project administration, Investigation. Kuan Hu: Writing − review & editing, Project administration, Investigation. Ming-Rong Zhang: Writing − review & editing, Writing − original draft, Visualization, Validation, Supervision, Project administration, Methodology, Investigation, Funding acquisition, Data curation, Conceptualization.

Conflicts of interest

The authors declare no conflicts of interest.

Appendix A. Supporting information

Supporting information to this article can be found online at https://doi.org/10.1016/j.apsb.2024.07.023.

References

1. Pavlova NN, Zhu J, Thompson CB. The hallmarks of cancer metabolism: still emerging. *Cell Metab* 2022;**34**:355−77.
2. Yoo HC, Yu YC, Sung Y, Han JM. Glutamine reliance in cell metabolism. *Exp Mol Med* 2020;**52**:1496−516.
3. Johmura Y, Yamanaka T, Omori S, Wang TW, Sugiura Y, Matsumoto M, et al. Senolysis by glutaminolysis inhibition ameliorates various age-associated disorders. *Science* 2021;**371**:265−70.
4. Simon J, Nuñez-García M, Fernández-Tussy P, Barbier-Torres L, Fernández-Ramos D, Gómez-Santos B, et al. Targeting hepatic glutaminase 1 ameliorates non-alcoholic steatohepatitis by restoring very-low-density lipoprotein triglyceride assembly. *Cell Metab* 2020;**31**:605−22.e10.
5. Du K, Hyun J, Premont RT, Choi SS, Michelotti GA, Swiderska-Syn M, et al. Hedgehog-yap signaling pathway regulates glutaminolysis to control activation of hepatic stellate cells. *Gastroenterology* 2018;**154**:1465−79.e13.
6. Gibb AA, Murray EK, Huynh AT, Gaspar RB, Ploesch TL, Bedi K, et al. Glutaminolysis is essential for myofibroblast persistence and *in vivo* targeting reverses fibrosis and cardiac dysfunction in heart failure. *Circulation* 2022;**145**:1625−8.
7. Ritterhoff J, Tian R. Metabolic mechanisms in physiological and pathological cardiac hypertrophy: new paradigms and challenges. *Nat Rev Cardiol* 2023;**20**:812−29.
8. Bradley CA. Glutamine-fuelled OXPHOS−a new target in MCL. *Nat Rev Cancer* 2019;**19**:363.
9. Li YJ, Zhang C, Martincuks A, Herrmann A, Yu H. STAT proteins in cancer: orchestration of metabolism. *Nat Rev Cancer* 2023;**23**:115−34.
10. Wettersten HI, Aboud OA, Lara Jr PN, Weiss RH. Metabolic reprogramming in clear cell renal cell carcinoma. *Nat Rev Nephrol* 2017;**13**:410−9.
11. Ding L, Xu X, Li C, Wang Y, Xia X, Zheng JC. Glutaminase in microglia: a novel regulator of neuroinflammation. *Brain Behav Immun* 2021;**92**:139−56.
12. Yuneva MO, Fan TW, Allen TD, Higashi RM, Ferraris DV, Tsukamoto T, et al. The metabolic profile of tumors depends on both the responsible genetic lesion and tissue type. *Cell Metab* 2012;**15**:157−70.
13. Yu D, Shi X, Meng G, Chen J, Yan C, Jiang Y, et al. Kidney-type glutaminase (GLS1) is a biomarker for pathologic diagnosis and prognosis of hepatocellular carcinoma. *Oncotarget* 2015;**6**:7619−31.
14. Li B, Cao Y, Meng G, Qian L, Xu T, Yan C, et al. Targeting glutaminase 1 attenuates stemness properties in hepatocellular carcinoma by increasing reactive oxygen species and suppressing Wnt/beta-catenin pathway. *EBioMedicine* 2019;**39**:239−54.
15. Canbay A, Sowa JP. L-Ornithine L-aspartate (LOLA) as a novel approach for therapy of non-alcoholic fatty liver disease. *Drugs* 2019;**79**:39−44.
16. Sappington DR, Siegel ER, Hiatt G, Desai A, Penney RB, Jamshidi-Parsian A, et al. Glutamine drives glutathione synthesis and contributes to radiation sensitivity of A549 and H460 lung cancer cell lines. *Biochim Biophys Acta* 2016;**1860**:836−43.
17. Gross MI, Demo SD, Dennison JB, Chen L, Chernov-Rogan T, Goyal B, et al. Antitumor activity of the glutaminase inhibitor CB-839 in triple-negative breast cancer. *Mol Cancer Ther* 2014;**13**:890−901.
18. Yuan L, Sheng X, Clark LH, Zhang L, Guo H, Jones HM, et al. Glutaminase inhibitor compound 968 inhibits cell proliferation and sensitizes paclitaxel in ovarian cancer. *Am J Transl Res* 2016;**8**:4265−77.
19. Kelloff GJ, Hoffman JM, Johnson B, Scher HI, Siegel BA, Cheng EY, et al. Progress and promise of FDG-PET imaging for cancer patient management and oncologic drug development. *Clin Cancer Res* 2005;**11**:2785−808.
20. Lodge MA. Repeatability of SUV in oncologic ^{18}F-FDG PET. *J Nucl Med* 2017;**58**:523−32.
21. Qu W, Zha Z, Ploessl K, Lieberman BP, Zhu L, Wise DR, et al. Synthesis of optically pure 4-fluoro-glutamines as potential metabolic imaging agents for tumors. *J Am Chem Soc* 2011;**133**:1122−33.
22. Qu W, Oya S, Lieberman BP, Ploessl K, Wang L, Wise DR, et al. Preparation and characterization of L-[5-^{11}C]-glutamine for metabolic imaging of tumors. *J Nucl Med* 2012;**53**:98−105.
23. Zhu L, Ploessl K, Zhou R, Mankoff D, Kung HF. Metabolic imaging of glutamine in cancer. *J Nucl Med* 2017;**58**:533−7.
24. Cohen AS, Grudzinski J, Smith GT, Peterson TE, Whisenant JG, Hickman TL, et al. First-in-human PET imaging and estimated radiation dosimetry of L-[5-^{11}C]-glutamine in patients with metastatic colorectal cancer. *J Nucl Med* 2022;**63**:36−43.
25. Fujinaga M, Kurihara Y, Ogawa M, Kumata K, Mori W, Zhang MR. P-137−simple and rapid automated synthesis of L-[^{11}C]glutamine. *Nucl Med Biol* 2022;**108−109**:S124−5.

26. Kawamura K, Hashimoto H, Ohkubo T, Hanyu M, Ogawa M, Nengaki N, et al. Automated radiosynthesis of [^{11}C]MTP38-a phosphodiesterase 7 imaging tracer-using [^{11}C]hydrogen cyanide for clinical applications. *J Labelled Comp Radiopharm* 2022;**65**:140−6.
27. Kleiner DE, Brunt EM, Van Natta M, Behling C, Contos MJ, Cummings OW, et al. Design and validation of a histological scoring system for nonalcoholic fatty liver disease. *Hepatology* 2005;**41**:1313−21.
28. Rosenberg AJ, Nickels ML, Schulte ML, Manning HC. Automated radiosynthesis of 5-[^{11}C]L-glutamine, an important tracer for glutamine utilization. *Nucl Med Biol* 2018;**67**:10−4.
29. Padakanti PK, Li S, Schmitz A, Mankoff D, Mach RH, Lee HS. Automated synthesis of [^{11}C]L-glutamine on Synthra HCN plus synthesis module. *EJNMMI Radiopharm Chem* 2019;**4**:5.
30. Hartwick EW, Curthoys NP. BPTES inhibition of hGA(124-551), a truncated form of human kidney-type glutaminase. *J Enzyme Inhib Med Chem* 2012;**27**:861−7.
31. Shukla K, Ferraris DV, Thomas AG, Stathis M, Duvall B, Delahanty G, et al. Design, synthesis, and pharmacological evaluation of bis-2-(5-phenylacetamido-1,2,4-thiadiazol-2-yl)ethyl sulfide 3 (BPTES) analogs as glutaminase inhibitors. *J Med Chem* 2012;**55**:10551−63.
32. Hebbard L, George J. Animal models of nonalcoholic fatty liver disease. *Nat Rev Gastroenterol Hepatol* 2011;**8**:35−44.
33. Xie L, Yui J, Hatori A, Yamasaki T, Kumata K, Wakizaka H, et al. Translocator protein (18 kDa), a potential molecular imaging biomarker for non-invasively distinguishing non-alcoholic fatty liver disease. *J Hepatol* 2012;**57**:1076−82.
34. Ibrahim SH, Hirsova P, Malhi H, Gores GJ. Animal models of nonalcoholic steatohepatitis: eat, delete, and inflame. *Dig Dis Sci* 2016;**61**:1325−36.
35. Sethi JK, Hotamisligil GS. Metabolic messengers: tumour necrosis factor. *Nat Metab* 2021;**3**:1302−12.
36. Harley IT, Stankiewicz TE, Giles DA, Softic S, Flick LM, Cappelletti M, et al. IL-17 signaling accelerates the progression of nonalcoholic fatty liver disease in mice. *Hepatology* 2014;**59**:1830−9.
37. Gillies RJ, Robey I, Gatenby RA. Causes and consequences of increased glucose metabolism of cancers. *J Nucl Med* 2008;**49**(Suppl 2):24s−42s.
38. Wilson M, Gill SK, MacPherson L, English M, Arvanitis TN, Peet AC. Noninvasive detection of glutamate predicts survival in pediatric medulloblastoma. *Clin Cancer Res* 2014;**20**:4532−9.
39. Goschzik T, Schwalbe EC, Hicks D, Smith A, Zur Muehlen A, Figarella-Branger D, et al. Prognostic effect of whole chromosomal aberration signatures in standard-risk, non-WNT/non-SHH medulloblastoma: a retrospective, molecular analysis of the HIT-SIOP PNET 4 trial. *Lancet Oncol* 2018;**19**:1602−16.
40. Venneti S, Dunphy MP, Zhang H, Pitter KL, Zanzonico P, Campos C, et al. Glutamine-based PET imaging facilitates enhanced metabolic evaluation of gliomas *in vivo*. *Sci Transl Med* 2015;**7**:274ra17.
41. Xie L, Hu K, Duo Y, Shimokawa T, Kumata K, Zhang Y, et al. Off-tumor IDO1 target engagements determine the cancer-immune set point and predict the immunotherapeutic efficacy. *J Immunother Cancer* 2021;**9**:e002616.
42. Wu Z, Zha Z, Li G, Lieberman BP, Choi SR, Ploessl K, et al. [^{18}F](2*S*,4*S*)-4-(3-Fluoropropyl)glutamine as a tumor imaging agent. *Mol Pharm* 2014;**11**:3852−66.
43. Lieberman BP, Ploessl K, Wang L, Qu W, Zha Z, Wise DR, et al. PET imaging of glutaminolysis in tumors by ^{18}F-(2*S*,4*R*)4-fluoroglutamine. *J Nucl Med* 2011;**52**:1947−55.
44. Ploessl K, Wang L, Lieberman BP, Qu W, Kung HF. Comparative evaluation of ^{18}F-labeled glutamic acid and glutamine as tumor metabolic imaging agents. *J Nucl Med* 2012;**53**:1616−24.
45. Huang Q, Stalnecker C, Zhang C, McDermott LA, Iyer P, O'Neill J, et al. Characterization of the interactions of potent allosteric inhibitors with glutaminase C, a key enzyme in cancer cell glutamine metabolism. *J Biol Chem* 2018;**293**:3535−45.
46. Soth MJ, Le K, Di Francesco ME, Hamilton MM, Liu G, Burke JP, et al. Discovery of IPN60090, a clinical stage selective glutaminase-1 (GLS-1) inhibitor with excellent pharmacokinetic and physicochemical properties. *J Med Chem* 2020;**63**:12957−77.
47. Yap TA, Dumbrava EE, Ahnert JR, Hong DS, Pant S, Karp DD, et al. First-in-human biomarker-driven phase I trial of the potent and selective glutaminase-1 (GLS1) inhibitor IACS-6274 (IPN60090) in patients (PTS) with molecularly selected advanced solid tumors. *J Clin Oncol* 2021;**39**:3001.
48. Lee CH, Motzer R, Emamekhoo H, Matrana M, Percent I, Hsieh JJ, et al. Telaglenastat plus everolimus in advanced renal cell carcinoma: a randomized, double-blinded, placebo-controlled, phase II ENTRATA trial. *Clin Cancer Res* 2022;**28**:3248−55.